arXiv:2005.14142v1 [cond-mat.str-el] 28 May 2020

Dirac-type nodal spin liquid revealed by machine learning

Yusuke Nomura[1,*] and Masatoshi Imada[2,3]

[1] *RIKEN Center for Emergent Matter Science, 2-1 Hirosawa, Wako, 351-0198, Japan*
[2] *Toyota Physical and Chemical Research Institute, 41-1 Yokomichi, Nagakute, Aichi, 480-1118, Japan*
[3] *Research Institute for Science and Engineering, Waseda University, 3-4-1 Okubo, Shinjuku-ku, Tokyo, 169-8555, Japan*

(Dated: April 22, 2025)

Pursuing fractionalized particles that do not bear properties of conventional bare particles such as electrons or magnons is a challenge in physics. Here we show that machine-learning methods for quantum many-body systems reveal the existence of a quantum spin liquid state with fractionalized spinons in spin-1/2 frustrated Heisenberg model convincingly, if it is combined with the state-of-the-art computational schemes known as the correlation ratio and level spectroscopy methods. The spin excitation spectra signal the emergence of gapless fractionalized spin-1/2 Dirac-type spinons in the distinctive quantum spin liquid phase. Unexplored critical behavior with coexisting power-law-decaying antiferromagnetic and dimer correlations emerges as well. The isomorph of excitations with the cuprate d-wave superconductors revealed here implies tight connection between the present spin liquid and superconductivity. This achievement manifests the power of machine learning for grand challenges in quantum many-body physics.

I. INTRODUCTION

Composite particles such as magnons and phonons consist of many elementary particles and provide us with fundamental understanding beyond the single-particle picture, where the spontaneous symmetry breaking and associated Nambu-Goldstone bosons are required in many cases. Fractionalization offers another route to realize emergent particles manifesting even in the absence of the symmetry breaking and serves as one of the central concepts in modern physics. The quark is the first example, where proton and neutron that had been considered to be elementary particles before have turned out each to be a composite particle of three quarks. Such emergent particles were also discovered in condensed matter in examples of polyacetylene soliton [1] and fractional quantum Hall states [2]. The expectation would be that the emergent particles arising from the fractionalization have particle character distinct from the bare electrons and then have novel functions in their many-body states, which may serve to future applications such as quantum computing.

Quantum spin liquid (QSL) is a potential platform of such a fractionalization, where suppressed magnetic order by geometrical frustration of the spin interaction is expected to drive the fractionalization. The QSL phase was theoretically proposed both through numerical supports and mean-field theories [3, 4]. Experimental efforts also supported the existence [4].

However, theoretical and experimental efforts have not yet identified and established the nature of fractionalized particles in reality due to its hidden character and various theoretical difficulties. So far, several different types of QSL have been proposed. These are classified, for example, by the spin excitation spectra, first whether the excitations are gapped [as in the cases of gapped Z_2 spin liquids (short-ranged resonating valence bond (RVB) states) [5, 6] and chiral spin liquid [7]], or gapless [8–14]. In the gapless case, one candidate is the gapless continuum of both of the singlet and triplet in an extended region of the Brillouin zone [10, 11], which may arise, for example, if spin-1/2 fermionic spinons emerging from the fractionalization constitute a large Fermi surface (or line) as in $U(1)$ spin liquid [12]. Another proposal is the spinon nodal liquid, where a small number of spinon gapless points appear in the Brillouin zone, resulting in the discrete gapless points of the observable spin excitation as well [13, 14] (see Fig. 6 shown later for illustration). At the gapless points, the dispersion may either be linear (Dirac dispersion) or quadratic.

To establish the real existence of the QSL and then narrow down the nature of the QSL, we need to identify excitation spectra connected to experimental indications for a proper Hamiltonian that really accommodates the QSL state. However, it remains a challenge because of highly competing energies of various quantum states. We need a highly accurate framework for both ground and excited states in a momentum-resolved fashion.

Such high accuracy is offered by a recently developed machine learning method for the ground state. Here, we extend this method to represent both the ground and excited states. To be more precise, we employ the restricted Boltzmann machine (RBM) combined with pair-product (PP) states [15]. The RBM+PP method is further consolidated by efficient two independent state-of-the-art numerical procedures, namely the correlation ratio [16] and level spectroscopy [17] methods, to reach the thermodynamic limit quickly by reducing the finite-size effect.

We then apply the RBM+PP to a candidate Hamiltonian of the spin-1/2 antiferromagnetic (AF) Heisenberg model on the square lattice with the nearest-neighbor

* yusuke.nomura@riken.jp

and next-nearest-neighbor exchange interactions, J_1 and J_2, respectively, called the J_1-J_2 Heisenberg model. We employ two independent analyses to settle down the controversy and obtain a firm evidence for the QSL phase: A finite range of the QSL phase in the region $0.49 \lesssim J_2/J_1 \lesssim 0.54$ is found. In the QSL phase, the singlet and triplet excitations are both gapless at four symmetric momenta in support of the nodal Dirac (or quadratic touching) dispersion of the fermionic spinon at $(\pm\pi/2, \pm\pi/2)$ in the Brillouin zone, which brings the coexisting power-law decay of spin-spin and dimer-dimer correlations. The isomorphic structure of the gapless excitations of spinons at $(\pm\pi/2, \pm\pi/2)$ with the d-wave superconducting state in the cuprate superconductors are suggestive of a mutual profound connection.

II. J_1-J_2 HEISENBERG MODEL ON SQUARE LATTICE

The two-dimensional (2D) J_1-J_2 Heisenberg Hamiltonian reads

$$\mathcal{H} = J_1 \sum_{\langle i,j \rangle} \mathbf{S}_i \cdot \mathbf{S}_j + J_2 \sum_{\langle\langle i,j \rangle\rangle} \mathbf{S}_i \cdot \mathbf{S}_j, \tag{1}$$

where $\mathbf{S}_i$ is the spin-1/2 operator at site i, whose α ($\alpha = x,\ y,\ z$) component is $S_i^\alpha = \frac{1}{2}\mathbf{c}_i^\dagger \sigma_\alpha \mathbf{c}_i$ with the electron operator $\mathbf{c}_i^\dagger = (c_{i\uparrow}^\dagger, c_{i\downarrow}^\dagger)$ and the Pauli matrix σ_α. We set $J_1 = 1$ as the energy unit and we restrict the parameter range as $0 \leq J_2 \leq 1$. $\langle i,j \rangle$ and $\langle\langle i,j \rangle\rangle$ denote nearest-neighbor and next-nearest-neighbor bonds, respectively.

Despite many numerical efforts, there exists controversy on the ground state of this model in the literature. Although it is clear that Néel- and stripe-type AF phases exist for small and large J_2 regions, respectively, the estimate of phase boundary around $J_2 = 0.5$, which is the classical boundary between the Néel and stripe phases, is still controversial. In fact, the issue is whether an unconventional quantum phase emerges around $J_2 = 0.5$. Possible phases proposed in the literature are QSL (either gapless [18, 19] or gapped [20]), valence bond solid (VBS) (either columnar [21] or plaquette [22]), or both of them [23, 24]. Deconfined quantum criticality was also proposed instead of the QSL phase [22, 25], which is interpreted as the QSL phase shrunk to a point and the fractionalization occurs only at this continuous phase transition point between the two symmetry-broken states. To settle the phase diagram, we need a highly accurate numerical method having flexible power to allow unbiased representations of quantum states.

III. METHODS

A. Machine learning for quantum many-body systems

Physical properties of many-body systems are governed by the eigenstates of the many-body Hamiltonian. Therefore, once the eigenstates of the Hamiltonian in Eq. (1) are known, we can predict the nature of the J_1-J_2 model precisely. However, there is difficulty in obtaining eigenstates because the dimension of the eigenstates grows exponentially as the system size increases. In the present case where we consider the J_1-J_2 Hamiltonian on the $L \times L$ ($= N_{\rm site}$) lattice with the periodic boundary condition, we cannot obtain the exact wave function when $N_{\rm site} \gtrsim 50$. However, by using machine learning techniques, we can compress the data of eigenstates and approximate the wave functions accurately with a finite number of parameters.

Here, we employ a newly developed machine learning method, RBM+PP [15], to obtain unbiased representations for both the ground and excited states. The RBM is a type of artificial neural network having two (visible and hidden) layers [26]. Using the machine learning technique, one can construct accurate many-body wave functions in an unbiased manner [27]. Indeed, it has been shown both theoretically and numerically that the RBM variational state flexibly describes a variety of quantum states [27–38], including the states exhibiting the volume-law entanglement entropy [28, 30], which is advantageous to represent not only the ground state but also the excited states. Indeed, the RBM is shown to accurately describe excited states of quantum spin Hamiltonians [37, 39], for which existing numerical methods often encounter numerical difficulties. Meanwhile, the PP state (called "geminal" in quantum chemistry) is represented by fermion wave functions, which can also accommodate volume-law entanglement. The PP state mapped onto bosonic spin space can represent RVB states [40], serving as a powerful starting point of the ground state approximation for the quantum spin systems [41]. The combined wave function, RBM+PP, inherits advantages of both and acquires much better accuracy than those achieved by either of RBM or PP state separately [15]. By the RBM+PP method with quantum number projections (see below), we can calculate momentum resolved excitations.

The RBM+PP wave function $\Psi(\sigma) = \langle \sigma | \Psi \rangle$ with $|\sigma\rangle = \prod_i c_{i\sigma}^\dagger |0\rangle$ is given by (we neglect normalization factor) [15]

$$\Psi(\sigma) = \phi_{\rm RBM}(\sigma)\psi_{\rm PP}(\sigma) \tag{2}$$

for each spin configuration $\sigma = (\sigma_1, \sigma_2, \ldots, \sigma_{N_{\rm site}})$ with $\sigma_i = 2S_i^z = \pm 1$. The number of sites is given by $N_{\rm site} = L \times L$ and the periodic boundary condition is assumed. The RBM part is given by (we omit irrelevant bias term

on the physical spins)

$$\phi_{\rm RBM}(\sigma) = \sum_{\{h_k\}} \exp\left(\sum_{i,k} W_{ik}\sigma_i h_k + \sum_k b_k h_k\right) \quad (3)$$

with the spin state of hidden units $h_k = \pm 1$, the interaction between physical and hidden variables W_{ik}, and the bias on the hidden variables b_k. The number of hidden units is taken to be $16N_{\rm site}$. The sum over hidden variables can be evaluated analytically and Eq. (3) can be efficiently computed as $\phi_{\rm RBM}(\sigma) = \prod_k 2\cosh(b_k + \sum_i W_{ik}\sigma_i)$. To make it possible to express the sign change of the wave function, we take the b_k and W_{ik} variational parameters to be complex. The PP state mapped onto spin systems reads

$$|\psi_{\rm PP}\rangle = P_{\rm G}\left(\sum_{i,j} f_{ij}^{\uparrow\downarrow} c_{i\uparrow}^\dagger c_{j\downarrow}^\dagger\right)^{N_{\rm site}/2} |0\rangle \quad (4)$$

with real variational parameters $f_{ij}^{\uparrow\downarrow}$. $\psi_{\rm PP}(\sigma)$ in Eq. (2) is related as $\psi_{\rm PP}(\sigma) \equiv \langle\sigma|\psi_{\rm PP}\rangle$. Here, $P_{\rm G} = \prod_i (1 - n_{i\uparrow}n_{i\downarrow})$ with $n_{i\uparrow} = c_{i\uparrow}^\dagger c_{i\uparrow}$ and $n_{i\downarrow} = c_{i\downarrow}^\dagger c_{i\downarrow}$ is the Gutzwiller projection prohibiting double occupancy.

We optimize the variational parameters $\{b_k, W_{ik}, f_{ij}^{\uparrow\downarrow}\}$ to minimize the energy $E = \frac{\langle\Psi|\mathcal{H}|\Psi\rangle}{\langle\Psi|\Psi\rangle}$. The energy is a highly nonlinear function with respect to the parameters $\{b_k, W_{ik}, f_{ij}^{\uparrow\downarrow}\}$. Therefore, by interpreting the energy as a loss function, the task of obtaining the lowest-energy state can be recast as a machine-learning task, namely a high-dimensional optimization problem of the highly nonlinear function (RBM+PP) using the highly nonlinear loss function (energy) [42]. The details of the optimization method and the calculation conditions can be found in Appendix A.

B. Strategy to overcome numerical challenges

Various competing controversial scenarios have been proposed for the phase diagram and the nature of possible QSL as we mentioned above. The machine learning only is, despite its crucial importance, not enough to resolve these controversies. In fact, even when we obtain accurate representations of quantum states by the machine learning, (i) another challenge is how to reach quick convergence to the thermodynamic limit from available finite-size results. Furthermore, provided that the QSL phase exists, the next challenge is to elucidate its nature; (ii) it is essential to estimate the excitation gap structure and momentum resolved dispersion accurately. To overcome the challenge (i), we employ a cross-check strategy by critically examining the consistencies of results from available completely independent cutting-edge methods. The best cross-check to our knowledge is offered by the combination of correlation ratio method (elucidating ground-state properties) [16] and level spectroscopy analysis (clarifying excited-state properties) [17], both of which have small system-size dependences. Remarkably, the former and the latter, though completely independent of each other, give very consistent results (see below). For (ii), we use quantum number projection to reach the accuracy on the spectroscopy level [43]. Here, we address the advantages of employing these methods.

1. *Correlation ratio*

Correlation ratio R quantifies how sharp the structure factor peak is. R is given by $R = 1 - S(\mathbf{Q} + \delta\mathbf{q})/S(\mathbf{Q})$ [16, 44], where $S(\mathbf{q})$ is the structure factor, $\mathbf{Q}$ is the peak momentum, and $\mathbf{Q}+\delta\mathbf{q}$ is the neighboring momentum. In the case of the square lattice, $\delta\mathbf{q} = (2\pi/L, 0)$ and $(0, 2\pi/L)$. We see that the R value approaches 1 (0) when the peak becomes sharp (broad). Therefore, with increasing system size, R scales to 1 in the ordered phase with delta-function Bragg peak and 0 in the disordered phase. The crossing point of R curves for different system sizes does not depend sensitively on system size. Thus it is suitable for an accurate estimate of the phase boundary between ordered and disordered phases in the thermodynamic limit [16, 44].

We examine R for both spin-spin and dimer-dimer correlations to detect Néel-AF and VBS transition points, respectively. The spin-spin correlation is given by $C_{\rm s}(\mathbf{r}_i - \mathbf{r}_j) = \langle \mathbf{S}_i \cdot \mathbf{S}_j\rangle$. The dimer-dimer correlation is defined as $C_{{\rm d}_\alpha}(\mathbf{r}_i - \mathbf{r}_j) = \langle D_i^\alpha D_j^\alpha\rangle - \langle D_i^\alpha\rangle\langle D_j^\alpha\rangle$ with the dimer operator $D_i^\alpha = \mathbf{S}_i \cdot \mathbf{S}_{i+\hat{\alpha}}$ on the nearest-neighbor bonds for the α-direction ($\alpha = x$, y). Hereafter, the subscripts "s", "d_x", and "d_y" are used for spin-spin, dimer-dimer ($\alpha = x$ and $\alpha = y$) correlations, respectively. Then, the structure factor is calculated from $S_\gamma(\mathbf{q}) = \frac{1}{N_{\rm site}}\sum_{i,j} C_\gamma(\mathbf{r}_i - \mathbf{r}_j) e^{i\mathbf{q}\cdot(\mathbf{r}_i - \mathbf{r}_j)}$ with $\gamma = \mathrm{s}$, d_x, and d_y. The two correlation ratios $R_{\rm Néel}$ and $R_{\rm VBS}$ are defined from $S_{\rm s}(\mathbf{q})$ and $S_{{\rm d}_x}(\mathbf{q})$ [or equivalently $S_{{\rm d}_y}(\mathbf{q})$] to determine the Néel-AF and VBS transition points, respectively. Close to the Néel-AF phase, the peak momentum is $\mathbf{Q} = (\pi, \pi)$ for $S_{\rm s}(\mathbf{q})$. For VBS, $\mathbf{Q} = (\pi, 0)$ for $S_{{\rm d}_x}(\mathbf{q})$ and $\mathbf{Q} = (0, \pi)$ for $S_{{\rm d}_y}(\mathbf{q})$.

2. *Level spectroscopy*

Quantum phases are characterized by their unique structure in excitation spectra. At finite sizes, if the phases are different, low-lying excitations will be characterized by different quantum numbers. Therefore, the transition point can be estimated by the size extrapolation of the crossing point of the low-lying excitation energies [17]. This level spectroscopy method is known to have small system size dependence as well. Indeed, it has played an important role in precisely determining the Berezinskii-Kosterlitz-Thouless transition point for the sine-Gordon model [17]. This method offers an analysis completely different but complementary to the correlation ratio method.

3. Quantum number projection

The eigenstates of the Hamiltonian in finite size systems are labeled by quantum numbers. By optimizing the RBM+PP wave function for each quantum number sector, we can obtain both the ground state and low-lying excited states. We apply total-momentum and spin-parity projections to the RBM+PP wave functions to specify the quantum number [43]:

$$\Psi^{S_\pm}_{\mathbf{K}}(\sigma) = \sum_{\mathbf{R}} e^{-i\mathbf{K}\cdot\mathbf{R}}[\Psi(T_{\mathbf{R}}\sigma) \pm \Psi(-T_{\mathbf{R}}\sigma)] \tag{5}$$

(double sign in the same order). S_+ (S_-) indicates even (odd) spin parity corresponding to even (odd) values of the total spin S. $\mathbf{K}$ is the total momentum. $T_{\mathbf{R}}$ is a translation operator shifting all the spins by $\mathbf{R}$. For each quantum number sector, we optimize the RBM+PP wave function to obtain the lowest-energy state. Although the spin-parity projection can only distinguish whether S is even or odd, we always obtain a singlet state for the even S sector and a triplet state for the odd S sector (we confirm it by calculating S expectation value for the obtained states). This is because the singlet (triplet) state is the lowest-energy state for each even (odd) S sector. We note that the quantum number projection is helpful not only to distinguish quantum numbers but also to lower the variational energy [45].

The ground state is given for $\mathbf{K} = (0,0)$ and even S sector. The energies for other quantum number sectors measured from the ground state energy determine the excitation spectra. Then, we can obtain singlet and triplet excitations separately with momentum resolution. Exceptionally, we need special treatments to obtain $S = 0$ excited state at $\mathbf{K} = (0,0)$ and $S = 2$ excited states, which are described in detail in Appendix A. As we mentioned above, the flexible representability of the RBM+PP gives accurate representations not only for ground states but also for excited states. The accurate estimate of momentum-resolved excitation gaps enables us to perform the above-mentioned level spectroscopy and also to elucidate the nature of the QSL phase.

C. Finite-size scaling method

Near the quantum critical point, the susceptibility χ at the ordering wave vector $\mathbf{Q}$ in finite-sized systems follow the following finite-size scaling form [46]

$$\frac{\chi(t,\mathbf{Q},L)}{L^{\gamma/\nu}} = f_\chi(L^{1/\nu}t), \tag{6}$$

where the universal scaling function f_χ appears with the correlation length exponent ν and the susceptibility exponent γ. Here, t assumed to satisfy $t \ll 1$ is the dimensionless distance to the critical point. In the present case $t = (J_2 - J_2^{\text{Néel}})/J_1$ or $t = (J_2 - J_2^{\text{VBS}})/J_1$. Through the relation between χ and the structure factor $S(t,\mathbf{Q},L)$ given by $\chi(t,\mathbf{Q},L) \sim S(t,\mathbf{Q},L)L^z$ with the dynamical exponent z, we find that the squared order parameter $m^2 = S(t,\mathbf{Q},L)/L^d$ for the d-dimensional system follows

$$m^2 L^{d+z-2+\eta} = f_\chi(L^{1/\nu}t), \tag{7}$$

if the Fisher's scaling relation $\gamma/\nu = 2 - \eta$ holds for η associated with the anomalous dimension characterized by the power-law decay of the correlation, $C(\mathbf{r}) \sim 1/r^{d+z-2+\eta}$ for distance $r = |\mathbf{r}|$ at the critical point. Then the finite-size scaling plot should exhibit the universal scaling function f_χ.

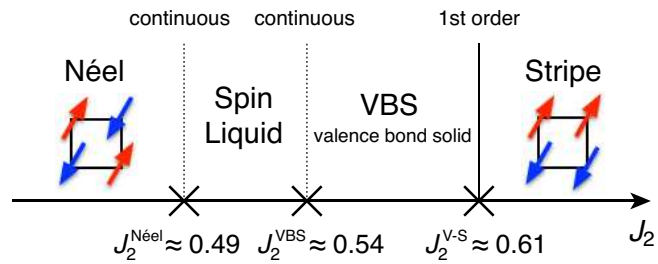

FIG. 1. Ground-state phase diagram of square-lattice J_1-J_2 Heisenberg model ($J_1 = 1$) obtained by the RBM+PP method.

IV. RESULTS

First, we check the accuracy of the RBM+PP method in analyzing the J_1-J_2 Heisenberg model (see Appendix B). We have confirmed that the RBM+PP achieves state-of-the-art accuracy not only among machine-learning-based methods but also among all available numerical methods. We have also found that the RBM+PP accurately represents excited states as well as the ground state.

A. Ground-state phase diagram

The RBM+PP method combined with the state-of-the-art numerical techniques convincingly uncovers the phase diagram of the J_1-J_2 Heisenberg model as shown in Fig. 1. In the small (large) J_2 region, the Néel-type (stripe) AF long-range order appears as in the classical phase diagram. In between these two phases, non-magnetic ground states, QSL and VBS, are found in the region $J_2^{\text{Néel}} \sim 0.49 \leq J_2 \leq J_2^{\text{VBS}} \sim 0.54$ and $J_2^{\text{VBS}} \sim 0.54 \leq J_2 \leq J_2^{\text{V-S}} \sim 0.61$, respectively. Whereas VBS breaks lattice symmetry, QSL does not break any. Clearly and notably, QSL is stabilized in a finite region of J_2 around $J_2 = 0.5$. The phase transition between VBS and stripe-AF at $J_2^{\text{V-S}}$ is of 1st order, which is characterized by the kink in the ground state energy, while

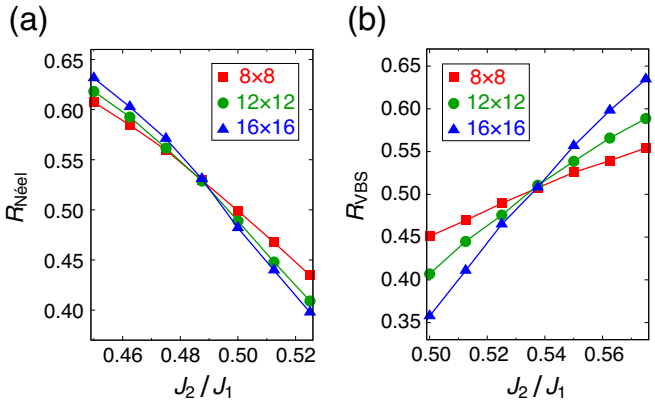

FIG. 2. System-size dependence of correlation ratio for (a) spin-spin and (b) dimer-dimer correlations, which are used to detect the phase boundary of Néel-AF and VBS, respectively.

the other two transitions are continuous (Fig. 12 in Appendix C). Below, we describe the procedure to determine the continuous phase transition points.

1. *Phase boundary determined by correlation ratio*

Results for the correlation ratios, $R_{\text{Néel}}$ and R_{VBS}, are shown in Figs. 2(a) and 2(b), respectively (see Figs. 13 and 14 in Appendix C for the raw data of correlation functions). We see clear crossings of curves for three sizes at nearly the same points at $J_2 = J_2^{\text{Néel}} \approx 0.49$ for $R_{\text{Néel}}$ and at $J_2 = J_2^{\text{VBS}} \approx 0.54$ for R_{VBS}. This standard procedure strongly supports that the two transitions associated with the Néel-AF and VBS ordering take place at the different points close to these system-size independent crossings. It supports the existence of an intermediate phase without any long-range ordering, i.e., QSL phase in the range $0.49 \lesssim J_2 \lesssim 0.54$.

2. *Phase boundary determined by level spectroscopy*

The level spectroscopy method was applied to the 2D J_1-J_2 Heisenberg model before [24]. They interpreted the crossing between the lowest singlet and triplet excitations as the VBS-order boundary, following Ref. 47. In addition, they found the singlet-quintuplet crossing and interpreted it as a signal of the disappearance of the AF long-range order, because the transition from the AF long-range order to quasi-long-range order in one-dimensional Heisenberg model with long-range interaction shows a similar behavior [24, 48]. These two crossings extrapolated to $L \to \infty$ limit gave different J_2 values: $J_2 = 0.463(2)$ and $J_2 = 0.519(2)$ for the singlet-quintuplet and singlet-triplet crossings, respectively.

To critically crosscheck the consistency with the above correlation ratio result, we also reexamine the level spectroscopy analysis as a complementary check. We here enjoy the advantage of the momentum resolution in addition [contrary to Ref. 24]. Figure 3 shows J_2 dependence of the excitation energies Δ for sizes (a) 12×12 and (b) 16×16 at high-symmetry momenta. The singlet-quintuplet and singlet-triplet crossings signaling the AF-QSL and QSL-VBS transitions, respectively, are highlighted by arrows. The size extrapolation of the crossing points is shown in Figure 4(a). We use L^{-2} scaling as in Refs. 24 and 47. The extrapolated thermodynamic values are $J_2 = 0.493(5)$ and $J_2 = 0.532(2)$ for the singlet-quintuplet and singlet-triplet crossings, respectively. The values are close to those of Ref. 24 above. Tiny differences may well be ascribed to the smaller system sizes calculated in Ref. 24 than ours.

More importantly, our phase boundary estimated by the level spectroscopy has a striking quantitative agreement with the correlation ratio result described above. It is of great significance to see the one-to-one correspondence between the ground-state phases and the excitation structures. We then safely conclude that a finite QSL region around $J_2 = 0.5$ emerges (see Supplementary Note 1 in Appendix D for additional noteworthy features found in level spectroscopy).

Figure 4(b) further shows the size dependence of the excitation gap Δ at the crossing points. $\Delta \times L$ seems to converge at a finite value as $L \to \infty$ for both crossings. Therefore, the two critical points corresponding to AF-QSL and QSL-VBS transitions become gapless in the thermodynamic limit with the scaling $\Delta \propto 1/L$.

B. Excitation spectrum in quantum spin liquid phase

As we see in Fig. 4(b), the singlet excitation with $\mathbf{K} = (\pi, 0)$ and $(0, \pi)$ becomes gapless at both AF-QSL and QSL-VBS critical points, implying that it is gapless through the QSL region sandwiched by these two critical points. In the QSL phase, the triplet excitation at $\mathbf{K} = (\pi, \pi)$ is the lowest excited state in finite-size systems [lower than the gapless singlet at $(\pi, 0)$] lending support to the vanishing gap also for (π, π) triplet in the thermodynamic limit. By the excitation involving the triplet at (π, π) and the singlet at $(\pi, 0)$, one can construct the triplet $(0, \pi)$, which must be gapless if these two elementary excitations are excited far apart in the thermodynamic limit, even when they are repulsively interacting. In a similar way, one can construct a gapless singlet excitation at (π, π) and $(0, 0)$. Therefore, the singlet and triplet excitations are both gapless at $(0, 0)$, $(\pi, 0)$, $(0, \pi)$ and (π, π).

To confirm this picture, we show in Fig. 5 the results for (a) singlet and (b) triplet excitation energies for 8×8, 12×12, and 16×16 lattices at $J_2 = 0.5$ in the QSL phase. We compute not only at high-symmetry $\mathbf{K}$ points $(0, 0)$, $(\pi, 0)$ and (π, π) but also at intermediate points $(\pi/2, 0)$, $(\pi, \pi/2)$ and $(\pi/2, \pi/2)$ [and symmetrically equivalent $\mathbf{K}$

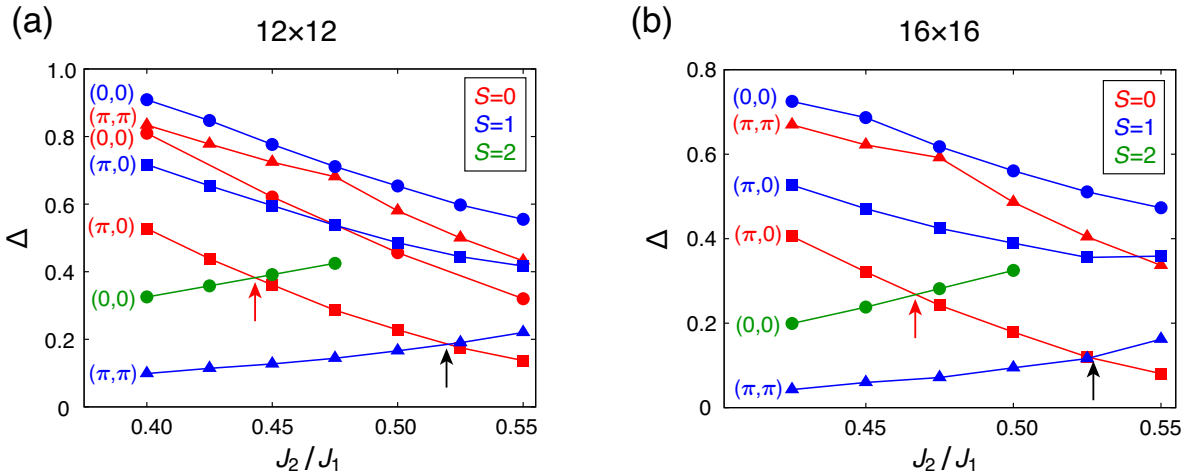

FIG. 3. Low-lying excitation energies for J_1-J_2 Heisenberg model for (a) 12×12 and (b) 16×16 lattices. The red and black arrows indicate singlet-quintuplet and singlet-triplet level crossings, respectively.

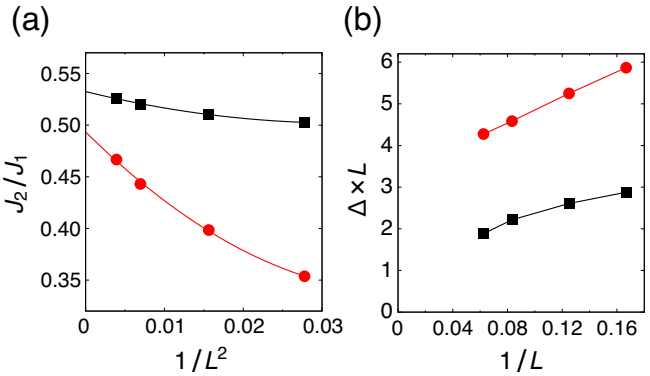

FIG. 4. (a) System-size dependence of singlet-quintuplet (red dots) and singlet-triplet (black squares) level crossings indicated by red and black arrows in Fig. 3. The extrapolation to the thermodynamic limit is done by the polynomial fit $a + b/L^2 + c/L^4$ (solid curves). (b) System-size dependence of the excitation gap Δ at the two level crossings.

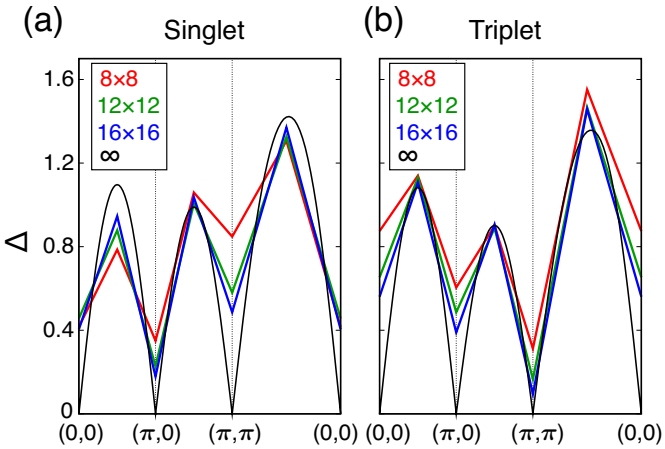

FIG. 5. Low-lying excitation in the QSL phase. (a) Singlet and (b) triplet excitation gap along the symmetric line in the Brillouin zone at $J_2 = 0.5$. On top of the high-symmetry $\mathbf{K}$ points $(0,0)$, $(\pi,0)$ and (π,π), the excitations at intermediate points $(\pi/2,0)$, $(\pi,\pi/2)$ and $(\pi/2,\pi/2)$ are calculated. Black curves are expected dispersions in the thermodynamic limit (see text).

points such as $(-\pi/2,0)$, $(0,\pi/2)$, $(0,-\pi/2)$ for $(\pi/2,0)$].

We find that the excitation gap decreases as L increases at the high-symmetry $\mathbf{K}$ points. The exceptional behavior at $\mathbf{K} = (0,0)$ in the singlet sector is presumably an artifact, which arises from numerical difficulty in obtaining excited states in $S = 0$ and $\mathbf{K} = (0,0)$ sector (Supplementary Note 2 in Appendix D). On the other hand, the gap stays nearly constant at the intermediate $\mathbf{K}$ points. By combining the gap analysis at the critical points (see above) and the size extrapolation of the gap by the scaling $a + b/L$ at the intermediate $\mathbf{K}$ points, we draw dispersion expected in the thermodynamic limit. The excitation spectra in the thermodynamic limit exhibit unconventional behavior in which the gap vanishes at the four high-symmetry momenta. We find only these four points as the gapless excitations suggesting Dirac-type linear dispersion around these four points. To corroborate the conclusion about the four Dirac-type gapless points in the QSL phase, we have also calculated the excitation energies at $(m\pi/3, n\pi/3)$ with $m, n = 0$, 1, 2, 3 for 12×12 lattice (Fig. 15 in Appendix C). From the limited momenta we studied, although other possibilities such as the higher-order dispersion (e.g., quadratic band touching) or tiny but extended gapless regions rather than points are not excluded, the results in Fig. 15 also support the Dirac-type nodal QSL.

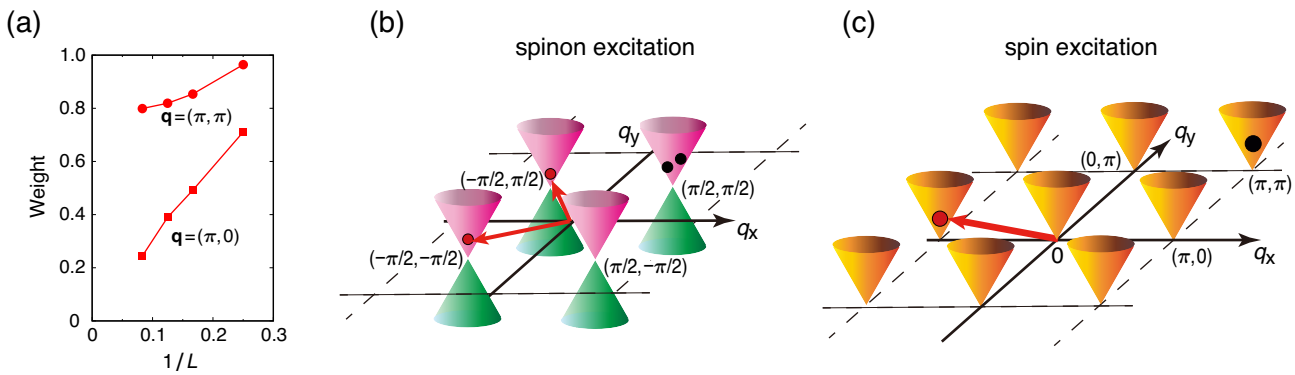

FIG. 6. (a) Weight of lowest branch in the dynamic spin structure factor for $\mathbf{q} = (\pi, 0)$ and (π, π) for $J_2/J_1 = 0.5$. At each $\mathbf{q}$ point, the weight is normalized by the total spectral weight $\int_0^\infty d\omega S_{\rm s}(\mathbf{q}, \omega)$. (b) Schematic picture for plausible spinon dispersion around gapless points $(\pm\pi/2, \pm\pi/2)$, illustrated both for particle (pink) and hole (green) sides above and below the spinon fermi energy. Two examples of two spinon excitations (two red and two black circles) are illustrated (see below). (c) The observable spin excitation is constructed from the two spinon excitations, which generates the gapless points at $(\pi, 0), (0, \pi), (0, 0)$ and (π, π). For instance, the red circle with the momentum around $(-\pi, 0)$ is constructed from the two spinon excitations shown as the small red circles with the momenta around $(-\pi/2, \pi/2)$ and $(-\pi/2, -\pi/2)$ in (b). The black circle is another example of spin excitation originated from the two spinon excitations shown as the small black circles in (b). Continuum incoherent spin excitations inside the cones are generated from the combinations of the two spinon excitations on the pink or green cone surfaces in (b).

C. Signature of fractionalization in quantum spin liquid

In the present QSL phase, one can expect an exotic fractionalization of particles, where a charge-neutral spin-1/2 excitation, called spinon, emerges. Although the spinon excitation cannot be detected experimentally, the evidence of the fractionalization can be detected as an incoherent continuum in the dynamic spin structure factor $S_{\rm s}(\mathbf{q}, \omega)$ (spin-1 excitation) [49], which is interpreted by the two-particle (two-hole) or particle-hole excitation continuum of the spinons. We here compute the weight in $S_{\rm s}(\mathbf{q}, \omega)$ at $\mathbf{q} = (\pi, 0)$ and (π, π) for the lowest triplet excitation shown in Fig. 5. If the excitation were the conventional magnon branch of a magnetic phase, the weight would be the order 1. If the weight vanishes, most of the weight lies in incoherent continuum at higher energies, supporting the emergence of fractionalized spinons [49].

Figure 6(a) shows the weight of the lowest branch in $S_{\rm s}(\mathbf{q}, \omega)$ for $\mathbf{q} = (\pi, 0)$ and (π, π). We indeed see that the weight decreases as the system size increases. In particular, the weight at $\mathbf{q} = (\pi, 0)$ rapidly decreases to zero, which means that the spectral weight is dominated by the incoherent continuum. [We do not analyze the behavior at $\mathbf{q} = (\pi, \pi)$ in detail because of a numerical challenge due to the proximity to AF(Néel)-QSL phase boundary $J_2 = J_2^{\rm Néel} \approx 0.49$ (Supplementary Note 3 in Appendix D)]. This is a strong evidence that the fractionalization indeed occurs in the QSL phase of the J_1-J_2 Heisenberg model. As we will discuss in Sec. V, the dispersion of the emergent fractionalized spinon is expected to be gapless at the points $(\pm\pi/2, \pm\pi/2)$ [Fig. 6(b)].

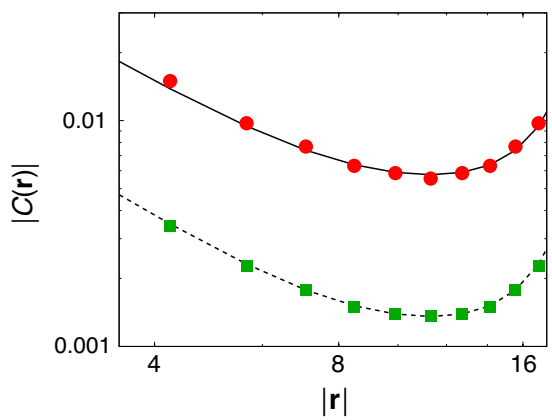

FIG. 7. Real-space spin-spin (red dots) and dimer-dimer (green squares) correlation functions, $|C_{\rm s}(\mathbf{r})|$ and $|C_{{\rm d}_x}(\mathbf{r})|$, respectively, for the diagonal direction ($r_x = r_y$) for 16×16 lattice at $J_2 = 0.5125$ in the QSL phase. The solid and dashed lines are proportional to the power-law decay $C(\mathbf{r}) \propto \frac{1}{|\mathbf{r}|^{z+\eta}} + \sum_{\mathbf{n}/=(0,0)} \left(\frac{1}{|\mathbf{r}-L\mathbf{n}|^{z+\eta}} - \frac{1}{|L\mathbf{n}|^{z+\eta}} \right)$ with $z + \eta = 1.52$ (solid) and 1.62 (dashed), in which we consider the effect of the periodic boundary condition [23]. The values of $z + \eta$ are taken from the analysis in Fig. 9(c). The upturn at large $|\mathbf{r}|$ is due to the periodicity of the lattice.

D. Real-space correlation functions in the quantum spin liquid phase

Figure. 7 shows the real-space decay of spin-spin and dimer-dimer correlation functions, $|C_{\rm s}(\mathbf{r})|$ and $|C_{{\rm d}_x}(\mathbf{r})|$, respectively, for the diagonal direction ($r_x = r_y$) for

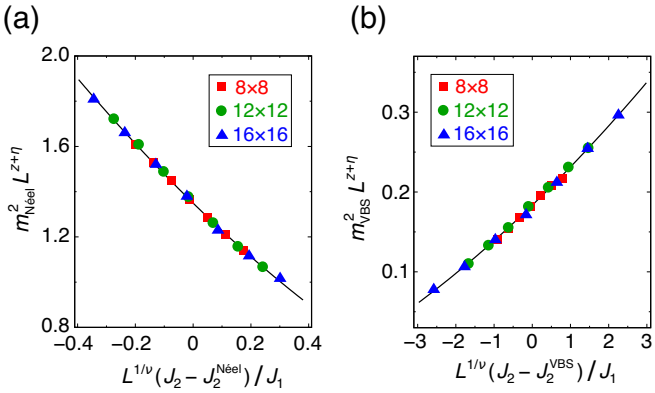

FIG. 8. Finite-size scaling analysis. (a) Data collapse for Nèel-AF order parameter. We assume $J_2^{\text{Néel}}/J_1 = 0.49$ and estimate the critical exponents $z+\eta$ and ν. The bayesian scaling analysis [50, 51] gives $z+\eta = 1.402(5)$ and $\nu = 1.29(7)$. (b) Data collapse for the VBS order parameter. The same analysis with assuming $J_2^{\text{VBS}}/J_1 = 0.54$ gives $z+\eta = 1.436(6)$ and $\nu = 0.67(2)$.

16×16 lattice in the QSL phase ($J_2 = 0.5125$) (for the definition of the correlation function, see Methods). If the correlation function shows power-law decay, it is expressed by the exponent $z+\eta$, namely the spin-spin and dimer-dimer correlations should show $C(\mathbf{r}) \sim r^{-(z+\eta)}$ ($r = |\mathbf{r}|$) in the real space as critical behavior. Both correlation functions indeed show consistent behaviors with the power-law decay. It evidences the critical nature of the QSL phase and is consistent with the gapless excitations clarified above.

E. Finite-size scaling and size dependence of order parameter

Figs. 8(a) and 8(b) show the data of finite-size scaling analysis of the Néel-AF and VBS order parameters, respectively. The squared order parameters for Néel-AF and VBS are given by $m^2_{\text{Néel}} = S_{\text{s}}(\mathbf{Q})/N_{\text{site}}$ with $\mathbf{Q} = (\pi,\pi)$ and $m^2_{\text{VBS}} = S_{\text{d}_x}(\mathbf{Q})/N_{\text{site}}$ with $\mathbf{Q} = (\pi, 0)$ [$= S_{\text{d}_y}(\mathbf{Q})/N_{\text{site}}$ with $\mathbf{Q} = (0,\pi)$], respectively [see Methods for the finite-scaling analysis method and the definition of the structure factor, $S_{\text{s}}(\mathbf{Q})$ and $S_{\text{d}_x}(\mathbf{Q})$]. For the Néel-AF and VBS orderings, we assume that the critical points are at $J_2^{\text{Néel}} = 0.49$ and $J_2^{\text{VBS}} = 0.54$, respectively (see the phase diagram in Fig. 1). The estimated critical exponents $z+\eta$ and ν deduced from the finite-size scaling are $z+\eta = 1.402(5)$ and $\nu = 1.29(7)$ for the Néel-AF order parameter, and $z+\eta = 1.436(6)$ and $\nu = 0.67(2)$ for the VBS order parameter, respectively [The estimate does not depend significantly on the values of $J_2^{\text{Néel}}$ and J_2^{VBS} (Supplementary Note 4 in Appendix D)]. These exponents do not belong to the known universality class and suggest unconventional criticality.

Figs. 9(a) and 9(b) show the size dependence of the Néel-AF and VBS order parameters, respectively. Solid black curves are expected scaling curve $m^2 \sim L^{-(z+\eta)}$ at the critical points obtained by employing $z+\eta = 1.402$ and 1.436 for the Néel-AF and VBS critical points, respectively.

V. DISCUSSION

The spin excitation dispersion has been rarely studied in the literature except for the studies obtained by assuming *a priori* a variational form of Z_2 nodal spin-liquid wave function [52, 53]. In Ref. 53, the spin cluster perturbation method is also employed to draw the dispersion. Our gapless structure lends support to these variational and the spin cluster perturbation studies in qualitative features, though our results have been obtained without such assumptions and approximations. Together with the consideration on the stability of the QSL phase [54] and the reason discussed below, our highly unbiased analysis evidences the QSL phase in the J_1-J_2 Heisenberg model characterized by Z_2 nodal QSL (rather than $U(1)$ QSL) with gapless and fractionalized spin-1/2 spinon excitations at $(\pm\pi/2, \pm\pi/2)$, proposed in an earlier study [18] (we did not exclude the possibility of $U(1)$ QSL just from the spin excitation spectra because the Z_2 and $U(1)$ QSL give very similar $S_{\text{s}}(\mathbf{q},\omega)$ [54]).

The real spin excitations measurable in experiments must be made of two-spinon excitations, and thus the singlet and triplet gapless points are $(0,0)$, $(\pi,0)$, $(0,\pi)$ and (π,π) [Fig. 6(c)]. As a result of the gapless singlet and triplet excitations, the spin-spin and dimer-dimer correlations decay algebraically in the real space in the QSL phase as we see above.

The finite-size scaling analysis shown above suggests that the value for critical exponent $z+\eta$ is about 1.4 for both of the AF-QSL and QSL-VBS critical points (Fig. 8), which is suggestive of an emergent symmetry between the spin-spin and dimer-dimer correlation. If the $U(1)$ QSL is realized as a phase, we will see the emergent symmetry within the whole QSL region as the critical phase [55, 56]. However, the power-law exponent $z+\eta$ seems to change in the QSL region: While it increases as J_2 increases for the spin-spin correlation, the dimer-dimer correlation shows the opposite trend [Fig. 9(c)]. It supports that the QSL with the emergent $U(1)$ symmetry is absent for an extended J_2 region and implies the extended region of the Z_2 QSL instead. From Fig. 9(c), $U(1)$ symmetry is deduced to emerge at a single point $J_2^{U(1)} \approx 0.52$, where the values of $z+\eta$ for the spin-spin and dimer-dimer correlations cross and coincide, and the Z_2 QSL may have different characters between $J_2 > J_2^{U(1)}$ and $J_2 < J_2^{U(1)}$. It will be of great interest to investigate this issue further in future, especially by considering more detailed system size dependence to further establish the thermodynamic behavior.

Since the excitation structure is isomorphic with the charge and spin excitations of the d-wave superconduct-

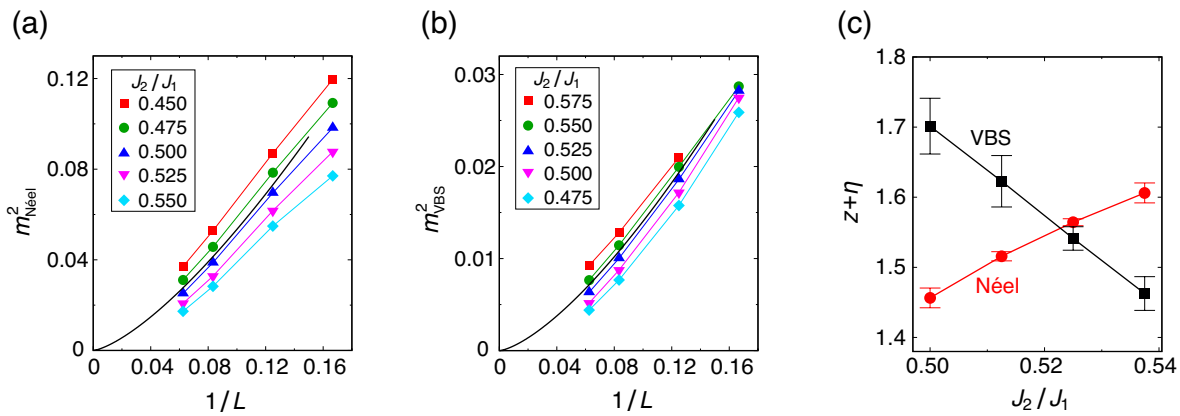

FIG. 9. Size dependence of the squared order parameters for (a) Nèel-AF and (b) VBS. The solid black curves in (a, b) are the expected size dependence at the critical point $m^2 \propto L^{-(z+\eta)}$ with $z+\eta$ estimated in Fig. 8. (c) J_2 dependence of the power-law exponent $z+\eta$ in the QSL phase obtained by fitting the size dependence of m^2 for $L = 8$, 12, 16 with a form $m^2 = AL^{-(z+\eta)}$ (A: constant).

ing state in the cuprate superconductors, it is suggestive of the connection of the two; the superconducting state could be borne out from the present QSL immediately when carriers are doped. The present accurate and unbiased estimate of the spinon excitation, especially, incoherent nature of the spin excitations with continuum, will provide insights into the unsolved puzzles of the cuprate superconductors including the incoherent transport and charge dynamics.

VI. SUMMARY

We have studied the 2D J_1-J_2 Heisenberg model using a highly accurate machine-learning method, RBM+PP, supplemented by the correlation ratio and level spectroscopy methods. By this combination, we have been able to extrapolate to the thermodynamic limit by two independent analyses and consistently reached the firm evidence for a finite QSL region around $J_2/J_1 = 0.5$. The phase diagram is summarized in Fig. 1. We have shown that the QSL is gapless (nodal) and the gap closes at the high symmetry points, consistently with the emergence of the fractionalized spin-1/2 spinons with gapless Dirac dispersion.

So far, the machine learning methods had been applied mostly to benchmark problems with known solutions. By extension to allow computation of excitations and dispersions and by combining with cutting-edge methods to reduce finite-size corrections, we have succeeded in uncovering QSL in the long-standing challenging problem. This achievement opens a new avenue of numerical methods applicable to the grand challenges of quantum many-body systems.

ACKNOWLEDGMENTS

We acknowledge useful discussions with Satoshi Morita, Anders W. Sandvik, and Zi Yang Meng. We also thank Satoshi Morita for providing us with the raw data in Ref. 23. Y.N. is grateful for fruitful discussions with Ribhu Kaul, Hidemaro Suwa, Yoshitomo Kamiya, Kenji Harada, Zheng-Cheng Gu, Giuseppe Carleo, and Ryui Kaneko. The implementation of the RBM+PP scheme is done based on the mVMC package [57]. The computation was mainly done at Supercomputer Center, Institute for Solid State Physics, University of Tokyo, and RIKEN K computer. The authors are grateful to the financial support by a Grant-in-Aid for Scientific Research (Grant No. 16H06345) from Ministry of Education, Culture, Sports, Science and Technology (MEXT), Japan. Y.N. was supported by Grant-in-Aids for Scientific Research (JSPS KAKENHI) (Grants No. 17K14336 and No. 18H01158). This work is financially supported by the MEXT HPCI Strategic Programs, and the Creation of New Functional Devices and High-Performance Materials to Support Next Generation Industries (CDMSI) as well as by "Program for Promoting Researches on the Supercomputer Fugaku" (Basic Science for Emergence and Functionality in Quantum Matter - Innovative Strongly-Correlated Electron Science by Integration of "Fugaku" and Frontier Experiments -). We also acknowledge the support provided by the RIKEN Advanced Institute for Computational Science under the HPCI System Research project (Grants No. hp170263, hp180170, hp190145 and hp200132).

Appendix A: Methods –Detail

Optimization of RBM+PP wave function

To search the lowest-energy quantum state for each quantum number sector, we optimize the variational parameters $\{b_k, W_{ik}, f_{ij}^{\uparrow\downarrow}\}$ to minimize the energy expectation value of the RBM+PP wave function. The energy expectation value $E = \frac{\langle\Psi|\mathcal{H}|\Psi\rangle}{\langle\Psi|\Psi\rangle}$ can be calculated by the Monte Carlo sampling with weight $p(\sigma) = \frac{|\Psi(\sigma)|^2}{\langle\Psi|\Psi\rangle}$

$$E = \sum_{\sigma} p(\sigma) E_{\rm loc}(\sigma), \tag{A1}$$

where the local energy $E_{\rm loc}(\sigma)$ is given by $E_{\rm loc}(\sigma) = \sum_{\sigma'} \langle\sigma|\mathcal{H}|\sigma'\rangle \frac{\langle\sigma'|\Psi\rangle}{\langle\sigma|\Psi\rangle}$. The E value depends on the variational parameters. To optimize the variational parameters to minimize E, we employ the stochastic reconfiguration (SR) method [58], which is equivalent to the imaginary-time Hamiltonian evolution $e^{-\tau\mathcal{H}}|\Psi\rangle$ within the Hilbert space spanned by the RBM+PP wave function. Because the imaginary-time Hamiltonian evolution $e^{-\tau\mathcal{H}}|\Psi\rangle$ always stably gives the lowest-energy state for each quantum number sector (as far as the initial RBM+PP state is not orthogonal to the lowest-energy state), the SR method enables stable optimizations. For further technical details of the SR optimization, we refer to Ref. 15.

The number of complex variational parameters in the RBM part is $N_{\rm hidden}$ for b_k and $N_{\rm hidden} \times N_{\rm site}$ for W_{ik}, respectively. As for the real variational parameters $f_{ij}^{\uparrow\downarrow}$ in the PP part for 8×8, 12×12, and 16×16 lattices, we impose 4×4 sublattice structure to reduce the number of parameters, whereas we do not employ sublattice structure for 6×6 lattice. In the case of 4×4 sublattice structure, the number of independent $f_{ij}^{\uparrow\downarrow}$ parameters is reduced from $N_{\rm site}^2$ to $4 \times 4 \times N_{\rm site} = 16N_{\rm site}$, and the other $f_{ij}^{\uparrow\downarrow}$ parameters are defined by spatial translation operations. In the presence of the Gutzwiller factor to map the PP state onto the spin system, the onsite $f_{ii}^{\uparrow\downarrow}$ parameters become completely redundant, i.e., the wave function does not depend on $f_{ii}^{\uparrow\downarrow}$ at all. Then, the number of relevant $f_{ij}^{\uparrow\downarrow}$ parameters are $16(N_{\rm site}-1)$. For the initial values for $\{b_k, W_{ik}, f_{ij}^{\uparrow\downarrow}\}$, we put random numbers in order not to introduce bias in the initial variational state.

Special treatments to obtain some specific excited states

As we describe in Sec. III B 3, we apply the spin-parity projection to distinguish whether the total spin S is even or odd. Because the singlet (triplet) state is the lowest state for each even (odd) S sector in the present study, we obtain a singlet (triplet) state for the even (odd) S sector. Therefore, we can obtain the singlet ($S = 0$) and triplet ($S = 1$) excited states with momentum resolution. However, we need special treatment to obtain $S = 0$ excited state at $\mathbf{K} = (0, 0)$ because the lowest-energy state in $S = 0$ and $\mathbf{K} = (0, 0)$ quantum number sector is the ground state. We use additional simplified point-group projection on top of those in Eq. (5) to obtain excited states belonging to different irreducible representation of the C_{4v} point group of the square lattice than that of the ground state as follows:

$$\Psi^{A,S_+}_{\mathbf{K}=(0,0)}(\sigma) = \Psi^{S_+}_{\mathbf{K}=(0,0)}(\sigma) + \Psi^{S_+}_{\mathbf{K}=(0,0)}(R_{\pi/2}\sigma) \tag{A2}$$

$$\Psi^{B,S_+}_{\mathbf{K}=(0,0)}(\sigma) = \Psi^{S_+}_{\mathbf{K}=(0,0)}(\sigma) - \Psi^{S_+}_{\mathbf{K}=(0,0)}(R_{\pi/2}\sigma), \tag{A3}$$

where the $R_{\pi/2}$ is an operator to rotate the spin configuration by 90 degrees. With this projection, we can distinguish whether the state belongs to A (either A_1 or A_2) irreducible representation or B (either B_1 or B_2) irreducible representation under the C_{4v} point group (to distinguish between A_1 and A_2 or between B_1 and B_2, we need full point group projection with 0, $\pi/2$, π, $3\pi/2$ rotations). The ground state corresponds to the former, while the excited state corresponds to the latter.

We also need special treatment to obtain $S = 2$ excited states. To this end, we use the mVMC (many-variable variational Monte Carlo method) [57] based on the PP wave function. In the mVMC, the full spin projection to specify the total spin is available, and we apply it to get $S = 2$ states. The full spin projection is time-consuming (at least about five times) compared to the spin-parity projection. At the cost of longer computational time for the full spin projection, the mVMC (only PP) gives comparable accuracy to the RBM+PP method.

Calculation conditions

In the present study, we fix the number of hidden units $N_{\rm hidden}$ to be $16N_{\rm site}$. We always apply the spin-parity and momentum projections during the optimization of the RBM+PP wave function. The special treatments to obtain $S = 0$ excited state at $\mathbf{K} = (0, 0)$ and $S = 2$ excited states are described above. To improve the quality of the data for the correlation function in Figs. 2, 6, 7, 8, 9, 13, and 14 quantitatively, we apply the simplified point-group projection in Eq. (A2) to the optimized ground state RBM+PP wave function for the sector with $S = 0$ and $\mathbf{K} = (0, 0)$. The ground state energy in Fig. 10 is also produced with the simplified point-group projection.

Appendix B: Benchmark

By applying the RBM+PP method to the 2D J_1-J_2 Heisenberg model on the square lattice, we confirm that the RBM+PP achieves state-of-the-art accuracy not only among machine-learning-based methods [59, 61–63] but

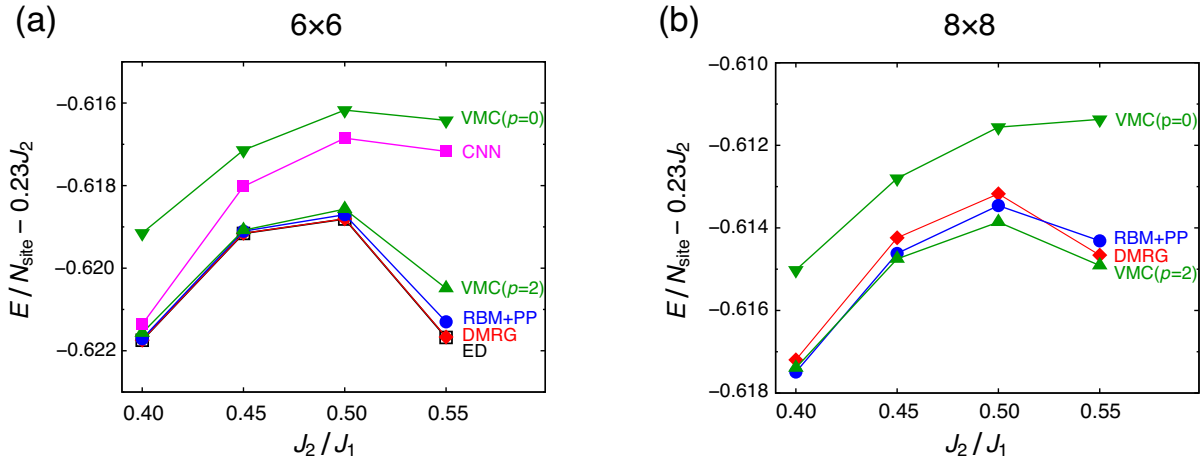

FIG. 10. Comparison of the ground state energy for the J_1-J_2 Heisenberg model. The comparison is made among the variational energies under the periodic boundary condition. The system sizes are (a) 6×6 and (b) 8×8. Our RBM+PP results are compared with those obtained by the variational Monte Carlo (VMC) method combined with the p-th order Lanczos steps [18], the density-matrix renormalization group (DMRG) (with 8182 SU(2) states) [22], the convolutional neural network (CNN) [59], and the exact diagonalization (ED) [60]. The CNN and ED results are available only for the 6×6 lattice.

TABLE I. Raw data of RBM+PP ground-state energy in Fig. 10.

	$J_2 = 0.40$	$J_2 = 0.45$	$J_2 = 0.50$	$J_2 = 0.55$
6×6	$-0.529709(5)$	$-0.515604(4)$	$-0.503704(5)$	$-0.494800(8)$
8×8	$-0.525492(4)$	$-0.511117(4)$	$-0.498460(6)$	$-0.48781(1)$

also among all available numerical methods. Figure 10 shows the comparison of the ground state energy among various methods (see Table I for the raw data). At $J_2 = 0.5$, where the frustration is strong, the relative error of the RBM+PP energy is as small as about 0.02 % for the 6×6 lattice. For the 8×8 lattice, the RBM+PP gives the best accurate energy among the compared methods at $J_2 = 0.4$. For $J_2 = 0.45$, 0.50 and 0.55, the best energy is achieved by the 2nd order Lanczos steps applied to the variational Monte Carlo (VMC) results [labeled as VMC($p = 2$) (with Lanczos) and VMC($p = 0$) (without Lanczos)]. The Lanczos method is well known for the efficient improvement of the energy; however, it does not necessarily improve other quantities such as the correlation functions. Also, the Lanczos method is computationally expensive. Therefore, although the Lanczos step can, in principle, be applied on top of the RBM+PP, we do not pursue it.

Remarkably, we also find that the RBM+PP accurately represents excited states as well as the ground state. Figure 11 shows the comparison of excitation energies for singlet, triplet, and quintuplet excitations between the exact and RBM+PP results for the 6×6 lattice. The agreement is excellent. Previously, there have been several attempts to obtain the excitation gap of the J_1-J_2 model [18, 20, 22, 24]. In Ref. 18, the excited states are

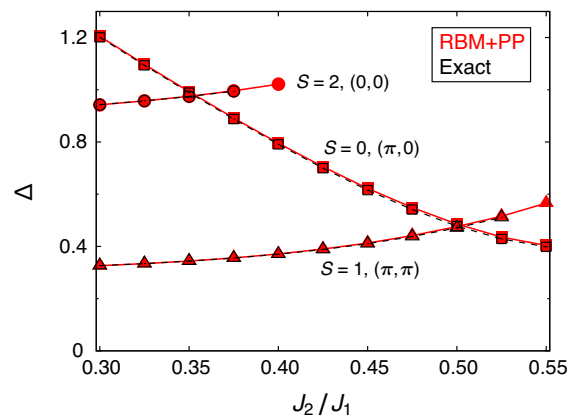

FIG. 11. Singlet, triplet and quintuplet excitation energies for 6×6 lattice obtained by RBM+PP (filled symbols) and ED (open symbols). In ED, we calculate up to five excited states using $\mathcal{H}\Phi$ [64]. At $J_2 = 0.40$, $S = 2$ excitation with the momentum $(0, 0)$ is not included in the five lowest excited states. The same holds for $S = 1$ excitation with the momentum (π, π) at $J_2 = 0.55$. The RBM+PP and exact results show a good agreement.

obtained by changing boundary condition, which limits the number of excited states that can be calculated [only $S = 2$ with the momentum $(0, 0)$ and $S = 0$ with $(\pi, 0)$ or $(0, \pi)$]. In Refs. 20, 22, and 24 using the density-matrix renormalization group (DMRG), the open boundary condition is employed, and hence the dispersion is not available because the momentum is ill-defined. In the present study, we can obtain accurate excitation energies with the momentum resolution. The accurate estimate of ex-

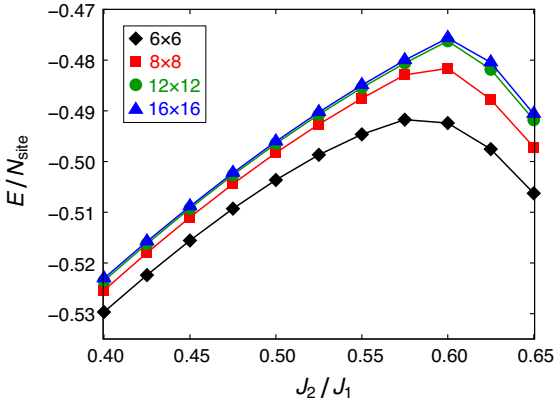

FIG. 12. J_2 dependence of RBM+PP ground-state energy of square-lattice J_1-J_2 Heisenberg model.

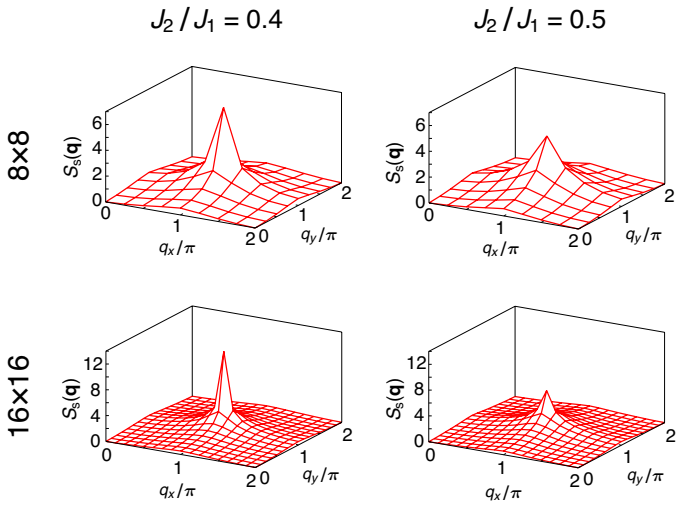

FIG. 13. Structure factor for spin-spin correlation $S_{\rm s}(\mathbf{q})$.

citation gaps enables us to perform the level spectroscopy to estimate the phase boundary and elucidate the nature of the QSL phase.

Appendix C: Supplementary data

Ground state energy

The phase transition between the VBS and stripe-AF phases at $J_2^{\text{V-S}}$ in Fig. 1 is of 1st order. To see this, we show the ground state energy as a function of J_2 in Fig. 12. As the system size increases, we see a clear kink in the energy curve at $J_2^{\text{V-S}} \approx 0.61$, giving evidence for the 1st-order phase transition.

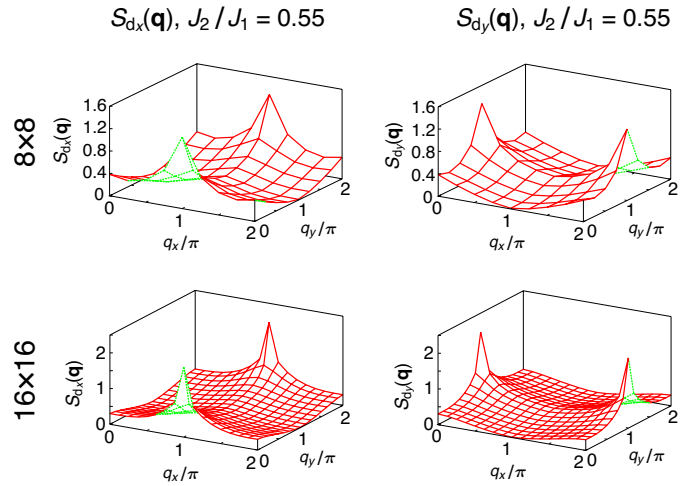

FIG. 14. Structure factor for dimer-dimer correlation $S_{\rm d_x}(\mathbf{q})$ and $S_{\rm d_y}(\mathbf{q})$.

Structure factors

In Sec. IV A 1, we discuss the crossing of the correlation ratio. The correlation ratio quantifies how sharp the structure factor peak is. In Figs. 13 and 14, we show the raw data of the structure factors for spin-spin and dimer-dimer correlations, respectively, which are used in the correlation ratio analysis.

Excitation gap at 12×12 lattice – sublattice-size dependence in the PP part

As we mention in Appendix A, we impose the 4×4 sublattice structure in the $f_{ij}^{\uparrow\downarrow}$ parameters in the PP part. With this setting, we have momentum resolution of 4×4 $\mathbf{K}$ points: $\mathbf{K} = (m\pi/2, n\pi/2)$ with $m, n = -1,\ 0,\ 1,\ 2$. To investigate the sublattice-size dependence, for 12×12 lattice, we also calculate the excitation energies using 6×6 sublattice structure. Then, we can calculate the excitation gaps at $\mathbf{K} = (m\pi/3, n\pi/3)$ with $m, n = -2$, -1, 0, 1, 2, 3.

Figure 15 shows the $f_{ij}^{\uparrow\downarrow}$-sublattice-size dependence of the excitation energies. We see that the excitation gaps at high-symmetry $\mathbf{K}$ points [$(0,0)$, $(\pi,0)$ and (π,π)] show good agreement between the 4×4 and 6×6 sublattice structures. At the intermediate $\mathbf{K}$ points, the excitation energies stay larger than those at high-symmetry $\mathbf{K}$ points. This fact supports the scenario of Dirac-type nodal QSL.

Appendix D: Supplementary Notes

1. Around the AF-QSL and QSL-VBS phase boundaries, we see noteworthy features in singlet exci-

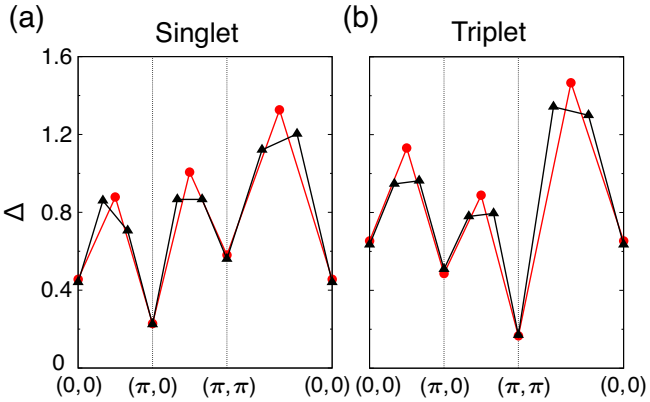

FIG. 15. $f_{ij}^{\uparrow\downarrow}$-sublattice-size dependence of excitation. (a) Singlet and (b) triplet excitation energy along the symmetric line in the Brillouin zone for 12×12 lattice. Red dots: 4×4 sublattice structure. Black triangles: 6×6 sublattice structure.

tations at $\mathbf{K} = (\pi, \pi)$ and triplet ones at $\mathbf{K} = (\pi, 0), (0, \pi)$. First, around the AF-QSL boundary ($J_2 = J_2^{\text{Néel}} \approx 0.49$), we see the kink in the excitation energy in the singlet $\mathbf{K} = (\pi, \pi)$ excitation [Figs. 3(a) and 3(b)]. Actually, there is a level crossing in this quantum number sector, and the point-group irreducible representation of the lowest state changes at the kink. Also around the QSL-VBS boundary ($J_2 = J_2^{\text{VBS}} \approx 0.54$), with increasing J_2, there is an upturn of the excitation energy of triplet $\mathbf{K} = (\pi, 0)$ excitation for 16×16 lattice [Fig. 3(b)], which seems consistent with the fact that the triplet excitation has a gap in the VBS phase. These two supplementary features are suggestive of the connection to the phase transitions; it would be interesting to investigate them further.

2. In Fig. 5, the excitation energy with $S = 0$ and $\mathbf{K} = (0, 0)$ sector stays almost constant as the system size L changes, in contrast with the behavior at the other high-symmetry $\mathbf{K}$ points. The singlet excited state at $\mathbf{K} = (0, 0)$ must belong to a different irreducible representation than that of the ground state, because, in the present method, we cannot obtain the excited states with the same irreducible representation as that of the ground state. Such excited states with the same irreducible representation might show similar behavior to those at the other high-symmetry $\mathbf{K}$ points.

3. The weight of the triplet at (π, π) seems to be scaled naturally to a nonzero value, which might imply the remnant of the pole. This requires further clarification in larger system sizes in future. The reason could partly be that the calculation is done close to the AF(Néel)-QSL phase boundary $J_2 = J_2^{\text{Néel}} \approx 0.49$. Another origin might be a possible anisotropic (elliptic) Dirac dispersion of spinons with preserved C_4 symmetry, which makes the spinon particle-hole excitation denser for the momentum transfer (π, π) and makes the slow convergence to zero.

4. The $J_2^{\text{Néel}}$ and J_2^{VBS} dependence of the estimate of the critical exponents is as follows. For the Néel-AF order parameter, $z + \eta = 1.379(4)$, $1.402(5)$, $1.428(5)$ and $\nu = 1.25(5)$, $1.29(7)$, $1.23(5)$ for $J_2^{\text{Néel}} = 0.485$, 0.490, 0.495, respectively. The ν values for different $J_2^{\text{Néel}}$ values agree within the size of error bars. Although $z+\eta$ increases as $J_2^{\text{Néel}}$ increases, the values lie around 1.4.

   For the VBS order parameter, $z + \eta = 1.471(8)$, $1.436(6)$, $1.400(5)$ and $\nu = 0.66(3)$, $0.67(2)$, $0.65(2)$ for $J_2^{\text{VBS}} = 0.535$, 0.540, 0.545, respectively. As in the case of the Néel-AF case, the ν values for different J_2^{VBS} values agree within the size of error bars.Though $z + \eta$ decreases slightly as J_2^{VBS} increases, it lies between 1.4 and 1.5, which are close to those at the Néel-AF critical point. Though $z+\eta$ decreases slightly as J_2^{VBS} increases, it lies between 1.4 and 1.5, which is close to those at the Néel-AF critical point.

[1] A. Heeger, S. Kivelson, J. R. Schrieffer, and W. P. Su, Rev. Mod. Phys. **89**, 781 (1988).
[2] R. B. Laughlin, Phys. Rev. Lett. **50**, 1395 (1983).
[3] L. Balents, Nature **464**, 199 EP (2010).
[4] Y. Zhou, K. Kanoda, and T.-K. Ng, Rev. Mod. Phys. **89**, 025003 (2017).
[5] X.-G. Wen, Phys. Rev. B **44**, 2664 (1991).
[6] N. Read and S. Sachdev, Phys. Rev. Lett. **66**, 1773 (1991).
[7] V. Kalmeyer and R. B. Laughlin, Phys. Rev. Lett. **59**, 2095 (1987).
[8] T. Kashima and M. Imada, J. Phys. Soc. Jpn. **70**, 3052 (2001).
[9] H. Morita, S. Watanabe, and M. Imada, J. Phys. Soc. Jpn. **71**, 2109 (2002).
[10] S.-S. Lee and P. A. Lee, Phys. Rev. Lett. **95**, 036403 (2005).
[11] T. Mizusaki and M. Imada, Phys. Rev. B **74**, 014421 (2006).
[12] N. Nagaosa and P. A. Lee, Rev. Mod. Phys. **78**, 17 (2006).
[13] L. Balents, M. P. A. Fisher, and C. Nayak, Int. J. Mod. Phys. **12**, 1033 (1998).
[14] T. Senthil and M. P. A. Fisher, Phys. Rev. B **62**, 7850 (2000).
[15] Y. Nomura, A. S. Darmawan, Y. Yamaji, and M. Imada,

Phys. Rev. B **96**, 205152 (2017).
[16] R. K. Kaul, Phys. Rev. Lett. **115**, 157202 (2015).
[17] K. Nomura, J. Phys. A **28**, 5451 (1995).
[18] W.-J. Hu, F. Becca, A. Parola, and S. Sorella, Phys. Rev. B **88**, 060402(R) (2013).
[19] W.-Y. Liu, S. Dong, C. Wang, Y. Han, H. An, G.-C. Guo, and L. He, Phys. Rev. B **98**, 241109 (2018).
[20] H.-C. Jiang, H. Yao, and L. Balents, Phys. Rev. B **86**, 024424 (2012).
[21] R. Haghshenas and D. N. Sheng, Phys. Rev. B **97**, 174408 (2018).
[22] S.-S. Gong, W. Zhu, D. N. Sheng, O. I. Motrunich, and M. P. A. Fisher, Phys. Rev. Lett. **113**, 027201 (2014).
[23] S. Morita, R. Kaneko, and M. Imada, J. Phys. Soc. Jpn. **84**, 024720 (2015).
[24] L. Wang and A. W. Sandvik, Phys. Rev. Lett. **121**, 107202 (2018).
[25] L. Wang, Z.-C. Gu, F. Verstraete, and X.-G. Wen, Phys. Rev. B **94**, 075143 (2016).
[26] P. Smolensky, *Parallel Distributed Processing: Explorations in the Microstructure of Cognition: Foundations* (MIT Press, Cambridge, 1986).
[27] G. Carleo and M. Troyer, Science **355**, 602 (2017), ISSN 0036-8075.
[28] D.-L. Deng, X. Li, and S. Das Sarma, Phys. Rev. X **7**, 021021 (2017).
[29] D.-L. Deng, X. Li, and S. Das Sarma, Phys. Rev. B **96**, 195145 (2017).
[30] J. Chen, S. Cheng, H. Xie, L. Wang, and T. Xiang, Phys. Rev. B **97**, 085104 (2018).
[31] I. Glasser, N. Pancotti, M. August, I. D. Rodriguez, and J. I. Cirac, Phys. Rev. X **8**, 011006 (2018).
[32] S. R. Clark, Journal of Physics A: Mathematical and Theoretical **51**, 135301 (2018).
[33] R. Kaubruegger, L. Pastori, and J. C. Budich, Phys. Rev. B **97**, 195136 (2018).
[34] S. Lu, X. Gao, and L.-M. Duan, Phys. Rev. B **99**, 155136 (2019).
[35] Y. Huang, and J. E. Moore, arXiv:1701.06246.
[36] T. Vieijra, C. Casert, J. Nys, W. De Neve, J. Haegeman, J. Ryckebusch, and F. Verstraete, Phys. Rev. Lett. **124**, 097201 (2020).
[37] Y. Nomura, J. Phys. Soc. Jpn. **89**, 054706 (2020).
[38] G. Carleo, I. Cirac, K. Cranmer, L. Daudet, M. Schuld, N. Tishby, L. Vogt-Maranto, and L. Zdeborová, Rev. Mod. Phys. **91**, 045002 (2019).
[39] K. Choo, G. Carleo, N. Regnault, and T. Neupert, Phys. Rev. Lett. **121**, 167204 (2018).
[40] P. W. Anderson, Science **235**, 1196 (1987), ISSN 0036-8075.
[41] S. Liang, Phys. Rev. B **42**, 6555 (1990).
[42] R. G. Melko, G. Carleo, J. Carrasquilla, and J. I. Cirac, Nature Physics **15**, 887 (2019).
[43] T. Mizusaki and M. Imada, Phys. Rev. B **69**, 125110 (2004).
[44] S. Pujari, T. C. Lang, G. Murthy, and R. K. Kaul, Phys. Rev. Lett. **117**, 086404 (2016).
[45] D. Tahara and M. Imada, J. Phys. Soc. Jpn. **77**, 114701 (2008).
[46] M. E. Fisher and M. N. Barber, Phys. Rev. Lett. **28**, 1516 (1972).
[47] H. Suwa, A. Sen, and A. W. Sandvik, Phys. Rev. B **94**, 144416 (2016).
[48] A. W. Sandvik, Phys. Rev. Lett. **104**, 137204 (2010).
[49] H. Shao, Y. Q. Qin, S. Capponi, S. Chesi, Z. Y. Meng, and A. W. Sandvik, Phys. Rev. X **7**, 041072 (2017).
[50] K. Harada, Phys. Rev. E **84**, 056704 (2011).
[51] K. Harada, Phys. Rev. E **92**, 012106 (2015).
[52] F. Ferrari and F. Becca, Phys. Rev. B **98**, 100405 (2018).
[53] S.-L. Yu, W. Wang, Z.-Y. Dong, Z.-J. Yao, and J.-X. Li, Phys. Rev. B **98**, 134410 (2018).
[54] X.-G. Wen, Phys. Rev. B **65**, 165113 (2002).
[55] M. Hermele, T. Senthil, and M. P. A. Fisher, Phys. Rev. B **72**, 104404 (2005).
[56] X. Y. Xu, Y. Qi, L. Zhang, F. F. Assaad, C. Xu, and Z. Y. Meng, Phys. Rev. X **9**, 021022 (2019).
[57] T. Misawa, S. Morita, K. Yoshimi, M. Kawamura, Y. Motoyama, K. Ido, T. Ohgoe, M. Imada, and T. Kato, Computer Physics Communications **235**, 447 (2019).
[58] S. Sorella, Phys. Rev. B **64**, 024512 (2001).
[59] K. Choo, T. Neupert, and G. Carleo, Phys. Rev. B **100**, 125124 (2019).
[60] H. J. Schulz, T. A. L. Ziman, and D. Poilblanc, J. Phys. I France **6**, 675 (1996).
[61] X. Liang, W.-Y. Liu, P.-Z. Lin, G.-C. Guo, Y.-S. Zhang, and L. He, Phys. Rev. B **98**, 104426 (2018).
[62] F. Ferrari, F. Becca, and J. Carrasquilla, Phys. Rev. B **100**, 125131 (2019).
[63] T. Westerhout, N. Astrakhantsev, K. S. Tikhonov, M. I. Katsnelson, and A. A. Bagrov, Nat. Commun. **11**, 1593 (2020).
[64] M. Kawamura, K. Yoshimi, T. Misawa, Y. Yamaji, S. Todo, and N. Kawashima, Computer Physics Communications **217**, 180 (2017), ISSN 0010-4655.